



HAL
open science

Safer and stronger together? Effects of the agglomeration on nanopowders explosion

Audrey Santandrea, Stéphanie Pacault, Sébastien Bau, Yohan Oudart, Alexis Vignes, Laurent Perrin, Olivier Dufaud

► To cite this version:

Audrey Santandrea, Stéphanie Pacault, Sébastien Bau, Yohan Oudart, Alexis Vignes, et al.. Safer and stronger together? Effects of the agglomeration on nanopowders explosion. *Journal of Loss Prevention in the Process Industries*, 2020, pp.104348. 10.1016/j.jlp.2020.104348 . hal-03060076

HAL Id: hal-03060076

<https://hal.science/hal-03060076>

Submitted on 13 Feb 2023

HAL is a multi-disciplinary open access archive for the deposit and dissemination of scientific research documents, whether they are published or not. The documents may come from teaching and research institutions in France or abroad, or from public or private research centers.

L'archive ouverte pluridisciplinaire **HAL**, est destinée au dépôt et à la diffusion de documents scientifiques de niveau recherche, publiés ou non, émanant des établissements d'enseignement et de recherche français ou étrangers, des laboratoires publics ou privés.



Distributed under a Creative Commons Attribution - NonCommercial 4.0 International License

23 tests were conducted respectively in a 20 L sphere and in a modified Hartmann tube. It was
24 observed that drying and/or sieving the nanocellulose mainly led to variations in terms of
25 ignition sensitivity but only slightly modified the explosion severity. In contrast, the
26 mechanical agglomeration of the silicon coated by carbon led to a great decrease in terms of
27 ignition sensitivity, with a minimum ignition energy varying from 5 mJ for the raw powder to
28 more than 1J for the agglomerated samples. The maximum rate of pressure rise also decreased
29 due to modifications in the reaction kinetics, inducing a transition from St2 class to St1 class
30 when agglomerating the dust.

31 **Keywords:** Dust explosion; Nanoparticles; Agglomeration; Dispersion

32

33

34 **1. Introduction**

35 According to the European Commission (2011/696/EU, 2011), a nanomaterial is “a natural,
36 incidental or manufactured material containing particles, in an unbound state or as an
37 aggregate or as an agglomerate and where, for 50% or more of the particles in the number size
38 distribution, one or more external dimensions is in the size range 1 nm – 100 nm”. This
39 recommendation also specifies that any material presenting a specific surface area by volume
40 of the material higher than $60 \text{ m}^2 \cdot \text{cm}^{-3}$ must be considered as a nanomaterial. This small size
41 induces additional, enhanced or different properties for the nanomaterials, which implies that
42 the fundamental properties such as chemical, mechanical, optical or biological properties are
43 modified and often innovative (Stark et al., 2015). Those new properties resulted to an
44 increasing interest in nanoparticles for applications in different fields, like health, automotive
45 industry, construction, food or electronic sector, but also generated a question concerning the

46 toxicity of the materials (Oberdörster et al., 2005). But nanoparticles, as well as any
47 combustible particles, present another important risk: their dispersion under certain conditions
48 and in the presence of an ignition source can lead to an explosion.

49 If dust explosion risks concerning micron-sized particles can be relatively well estimated, it is
50 not yet the case for nanoparticles. Indeed, the interest in nanotechnologies and in their specific
51 properties is quite recent and there are only a few feedbacks on accidental dust explosions
52 involving nanoparticles (Wu et al., 2014). Some laboratory tests were already carried out to
53 evaluate the ignition sensitivity and explosivity of nanopowders (Boillard et al., 2013;
54 Holbrow et al., 2010; Krietsch et al., 2015; Wu et al., 2009). It appears that powders are
55 usually more sensitive to ignition, but no significant variation concerning the explosion
56 severity was observed (Bouillard et al., 2010; Dufaud et al., 2011; Holbrow et al., 2010). This
57 phenomenon is mainly explained by the agglomeration and aggregation phenomenon induced
58 by the small size of the nanoparticles, which reduces the reactive surface area and decreases
59 the explosion severity (Eckhoff, 2011, 2012).

60 Generally, a nanopowder is comprised of primary nanoparticles, i.e. individual nanoparticles,
61 which aggregate, forming so-called “primary aggregates”, which themselves agglomerate
62 with each other. An agglomerate consists of weakly bonded particles that can be separated
63 while an aggregate is an assembly of strongly bonded particles that cannot be broken
64 (Sokolov et al., 2015; Walter, 2013). The main cohesion forces inducing the agglomeration of
65 nanoparticles aggregates are the van der Waals interactions, electrostatic and magnetic forces,
66 and, in the case of wet particles, capillary effects (Debrincat et al., 2008; Hartley et al., 1985).
67 Each agglomerate then possesses a cohesion strength that can be calculated by different ways
68 (Kendall, 1988; Rumpf, 1962; Weiler et al., 2010). In order to break an agglomerate, an
69 energy higher than the cohesion strength must be provided, leading back to the primary
70 aggregates.

71 For an explosion to occur, some conditions are needed. Among them is the dispersion of the
72 powder, which can break the agglomerates, at least partially, depending on the shear stress
73 occurring during the dust dispersion. Since the particle size distribution (PSD) is a very
74 important parameter influencing dust explosion, it becomes necessary to characterize the dust
75 cloud not only before its dispersion, but also at the exact ignition time (Santandrea et al.,
76 2019b). Moreover, it is imperative to choose wisely the operating conditions for the explosion
77 tests, to be sure to evaluate the worst -but realistic- case scenario. Indeed, the standard
78 conditions were established for micron-sized particles and are currently applied when testing
79 nanoparticles. However, these conditions may need to be adapted due to the specific
80 properties of nanomaterials (Santandrea et al., 2020).

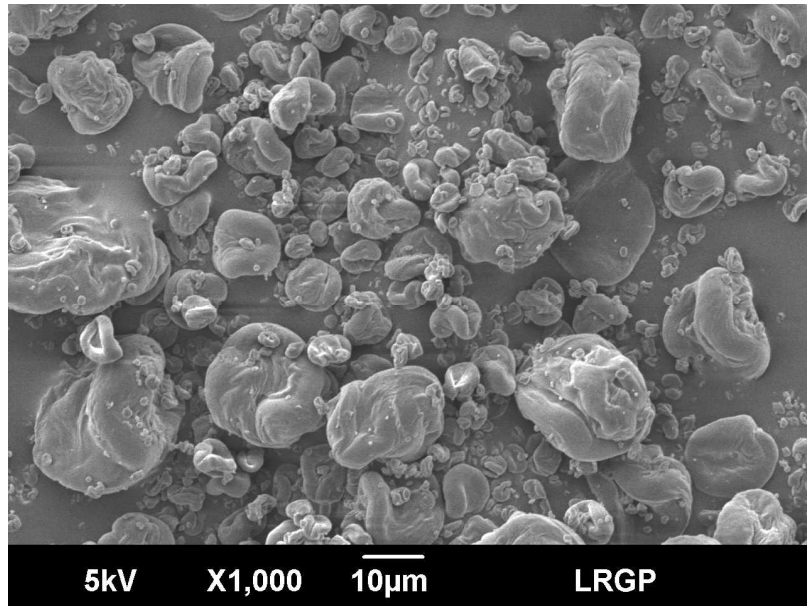
81 The impact of the agglomeration on the explosion severity of nanopowders was evaluated by
82 modifying the agglomerates size and cohesion strength before their dispersion and performing
83 explosion tests in a 20 L sphere according to international standards (EN 14034-1, 2004; EN
84 14034-2, 2006). Since the addition of a cohesive agent would modify the reactions involved
85 in the explosion, three main ways can be considered: grinding, selection (sieving), and
86 mechanical agglomeration (e.g. wet or dry granulation, compaction). The dispersion
87 procedure in the 20 L sphere already inducing a high shear stress due to the pressurization of
88 the dust container at 20 barg, it would be difficult to further reduce the size of the
89 agglomerates after dispersion. Indeed, the smaller the particle (or agglomerate), the harder it
90 is to be broken (Deng et al., 2016). Moreover, dry powder grinding would not allow to obtain
91 agglomerates smaller than around 1 μm , and the process would produce heat and possibly
92 electrostatic discharges that could be sufficient to ignite the most sensitive powders.
93 Therefore, powder grinding was not considered as a suitable solution. The effects of the
94 agglomeration on the explosion severity and ignition sensitivity were then investigated by

95 sieving and by mechanical agglomeration, respectively on nanocellulose and carbon coated
96 silicon powders.

97 **2. Materials and methods**

98 **2.1. Materials**

99 The effects of nanopowders agglomeration on their explosivity were investigated using two
100 different materials. First, a nanocrystalline cellulose (NCC from CelluForce), called
101 ‘nanocellulose’, was chosen due to its organic nature and wide range of applications. This
102 powder is constituted of primary nanofibers of 3 nm width and an average length of 70 nm
103 which form agglomerates with diameters ranging between 1 μm and several dozens of
104 micrometers, as presented in Figure 1. To avoid the influence of humidity on both
105 agglomeration state (capillary effects) and explosion characteristics, which was discussed by
106 Santandrea et al. (2020), this powder was systematically dried at 90°C under vacuum. The
107 water activity, i.e. the partial vapor pressure of water divided by the standard state partial
108 vapor pressure of water, was measured around 0.03 after drying (Aw-meter, Rotronic),
109 confirming that no additional water present in the powder would participate to the
110 combustion. In an attempt to obtain different agglomerate sizes, the nanocellulose was sieved
111 using a 40 μm mesh strainer submitted to low amplitude vibrations to avoid the breakage of
112 the agglomerates. This procedure then allows the separation of the biggest agglomerates from
113 the finest particles.



114

115

Figure 1. Raw nanocellulose observed by Scanning Electron Microscopy

116

Complementary to the PSD selection performed on nanocellulose, the effects of a mechanical

117

agglomeration without any additive were investigated on carbon coated silicon, noted 'Si Ω C',

118

through different agglomerated samples directly supplied by Nanomakers. Due to the low

119

density of the nanoparticles, such modification notably facilitates the transportation of the

120

powder and increases the powder flowability. Contrary to the nanocellulose, the powder was

121

not dried to avoid the breakage of the agglomerates, as the mechanical agglomeration was

122

realized directly on the raw powder without any additive. Moreover, the oxidation of silicon

123

in the presence of water can lead to the formation of hydrogen (Mehta et al., 2014), which

124

would increase the explosion severity. In this case, drying the powder would probably lead to

125

an underestimation of the safety parameters of the powders.

126

Four samples of carbon coated silicon constituted of the same powder with different densities,

127

agglomerates sizes and cohesion strengths were then studied in this work: the raw powder of

128

primary diameter of 40 nm and density of 40 g.L⁻¹, two samples agglomerated according to a

129

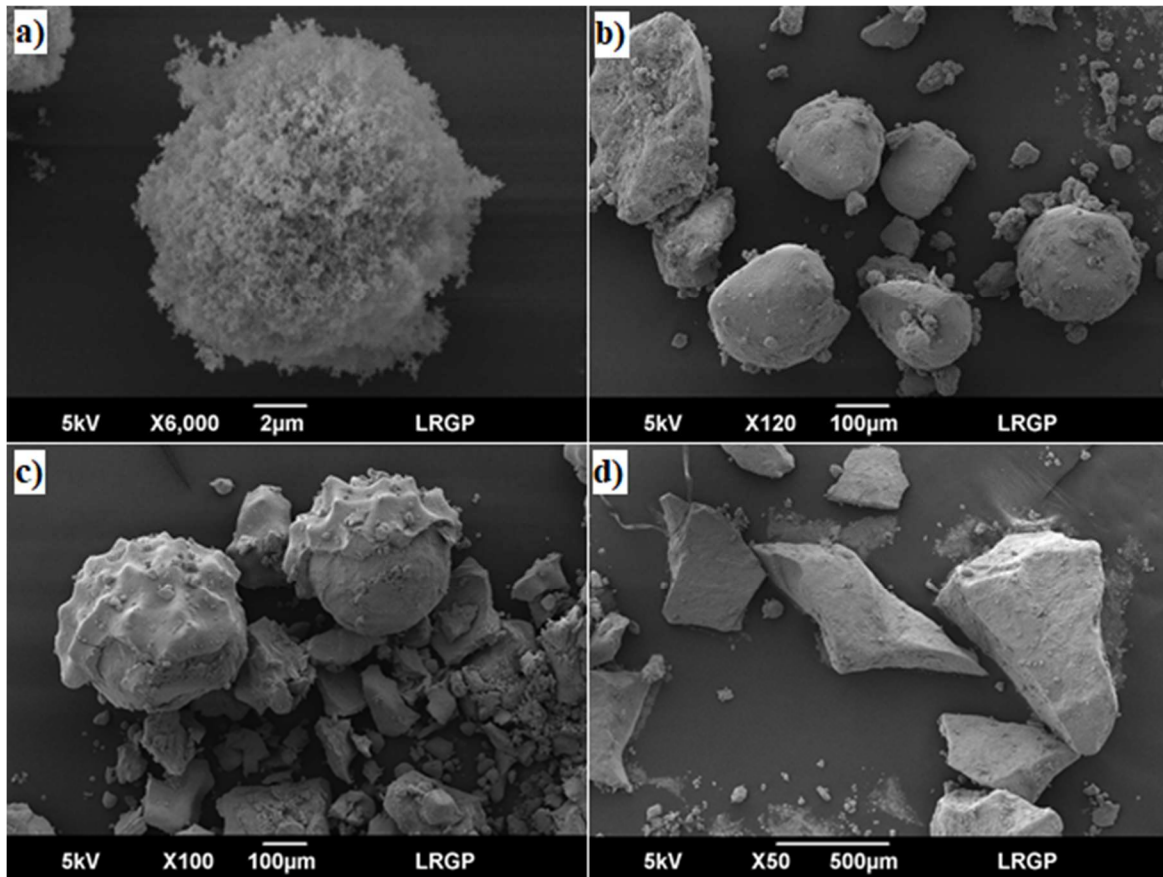
process noted 'process A' with bulk densities of respectively 260 g.L⁻¹ and 400 g.L⁻¹, which

130

will be noted powders A1 and A2, and a sample agglomerated according to a 'process B' with

131 a bulk density of 400 g.L^{-1} , noted sample B. The specific processes of agglomeration are
132 confidential and unfortunately cannot be described here. Scanning Electron Microscopy
133 analyses were performed on each sample, without any modification, to visualize the shape
134 modifications due to the agglomeration (Figure 2).

135 The raw powder appears to be constituted of small spherical agglomerates of apparent
136 diameters lower than $10 \mu\text{m}$, as shown in Figure 2a. The modified powders also present the
137 same kind of agglomerated structures, but also bigger agglomerates. Indeed, the powder A1
138 seems essentially composed of big 'roughly spherical' agglomerates with a diameter around
139 100 to $200 \mu\text{m}$ (Figure 2b). Similar agglomerates can be found in the sample A2, but with
140 agglomerates size around $300 \mu\text{m}$ (Figure 2c). Finally, when using the process B to
141 agglomerate the powder, non-spherical agglomerates with an average size reaching $500 \mu\text{m}$
142 were formed (Figure 2d).



143

144 *Figure 2. Carbon-coated silicon observed by Scanning Electron Microscopy a) Raw powder*

145 *b) Sample A1 (260 g.L⁻¹) c) Sample A2 (400 g.L⁻¹) d) Sample B (400 g.L⁻¹)*

146 **2.2. Methods**

147 The initial particle size distribution (PSD), i.e. before dispersion in the testing equipment, of
 148 each sample of nanocellulose and carbon coated silicon was measured in air using a laser
 149 diffraction HELOS/KR-Vario (Sympatec GmbH). The PSD was characterized by
 150 sedimentation of the powders in the measuring area of the apparatus. As this process was
 151 realized manually (by sprinkling powders with a spatula shaken at a constant height), it may
 152 therefore be questioned in terms of repeatability. Nevertheless, several tests on each sample
 153 led to similar PSD, which then gives a good order of magnitude of the PSD of the dust cloud
 154 submitted to very low shear rates. In this study, the surface fraction was considered instead of
 155 the ‘commonly-used’ volume fraction when analyzing the PSD in order to highlight the

156 surface specificities of nanoparticles. Moreover, when considering the volume fraction, the
157 high volume of big agglomerates tends to occult the presence of smaller nano-agglomerates.
158 Thus, the volume fraction measured by the apparatus was converted into a surface fraction
159 using the equivalent volume diameter.

160 Since the dispersion procedure, required to produce a dust explosion induces a shear stress
161 that can potentially break the agglomerates, PSD measurements were conducted after
162 dispersion in the explosion vessel. However, no apparatus or technique currently allow the
163 determination of a PSD over a wide range from 10 nm (primary particles) to 500 μm
164 (agglomerates), at high concentration (above the lower explosion limit or at least at a few $\text{g}\cdot\text{m}^{-3}$)
165 and at high frequency (each millisecond or at least each 10 ms). Thus, different techniques
166 were combined. The dust dispersion was realized in a 20 L sphere equipped with windows
167 according to the same procedure than during explosion tests: the weighed sample is placed in
168 the dust container, and the sphere is evacuated to 0.4 bara. The container is then pressurized
169 20 barg and the electrovalve connecting the dust canister to the explosion chamber opens,
170 inducing the dispersion of the powder. Contrary to explosion tests, no ignition was performed,
171 and the time evolution of the PSD was recorded.

172 The laser diffraction sensor (Helos - Sympatec) used to measure the initial PSD of the dust
173 before dispersion was attached to the 20 L sphere equipped with visualization windows made
174 of borosilicate with a diameter of 9.7 cm to allow optical measurements (Murillo, 2016). The
175 PSD was then measured at the place of ignition using various lenses (called R1, R3 and R5)
176 and systematically presented at the moment of ignition, i.e. 60 ms after the beginning of the
177 dispersion according to EN 14034 1&2 (2004; 2006). The boundaries of the measurement
178 ranges are 0.1 – 35 μm , 0.5 – 175 μm and 0.5 – 875 μm for R1, R3 and R5 lenses,
179 respectively. It should be noted that the maximum distance between the lens and the sample is
180 20 mm for R1, whereas it can reach 47 cm for R5. As a consequence, only the powder located

181 near the observation windows will be analyzed by using R1, whereas the other lenses will
182 give a PSD representative of the overall content of the sphere.

183 The presence of nanoparticles after dispersion of nanocellulose and carbon coated silicon in
184 the 20 L sphere was also investigated using a Fast Mobility Particle Sizer (FMPS - TSI)
185 measuring electrical mobility diameters from 5.6 to 560 nm with 1 Hz time resolution and a
186 Scanning Mobility Particle Sizer (SMPS), providing one measurement every two minutes.
187 Despite the low frequency and mass concentration which prevent an accurate characterization,
188 the observation of nanoparticles up to two minutes after dispersion, with particle size
189 distribution ranging from 10 to 400 nm, implies that such particles were also present a few
190 dozens of milliseconds after dispersion.

191 The explosion severity of each sample was measured in a standard 20 L sphere according to
192 EN 14034 1&2 (2004; 2006), i.e. using two chemical igniters of 5 kJ each and an ignition
193 delay time, t_v of 60 ms. The 20 L sphere is equipped with a cooling jacket with water at 300
194 K. The minimum ignition energy (MIE) of the samples was measured using a standard
195 modified Hartmann tube according to ISO/IEC 80079-20-2 (2016). Although international
196 standards EN 14034-3 (2006) recommend to measure the lower explosion limit in the 20 L
197 sphere using an ignition energy of 2 kJ, this parameter was approximated in the same
198 conditions as the explosion severity tests, i.e. for an ignition energy of 10 kJ.

199 **3. Results and discussions**

200 **3.1. Effects of particle size selection: example of nanocellulose**

201 As detailed in section 2.1, the nanocellulose was dried and sieved using a 40 μm mesh
202 strainer. The particle size distribution of each fraction was measured using the laser
203 diffraction sensor (R3 lens) by sedimentation. The upper fraction was constituted of
204 agglomerates of sizes between 40 and 100 μm , whereas the lower fraction exhibited a surface

205 diameter around 10 μm . The agglomerates sizes of each sample are summarized in Table 1. It
 206 should be noted that the sieving process does not modify the size of the agglomerates and
 207 only aims at separating the agglomerates according to their sizes. However, the biggest
 208 agglomerates, i.e. the less cohesive, may be broken during the sieving process (Deng et al.,
 209 2016).

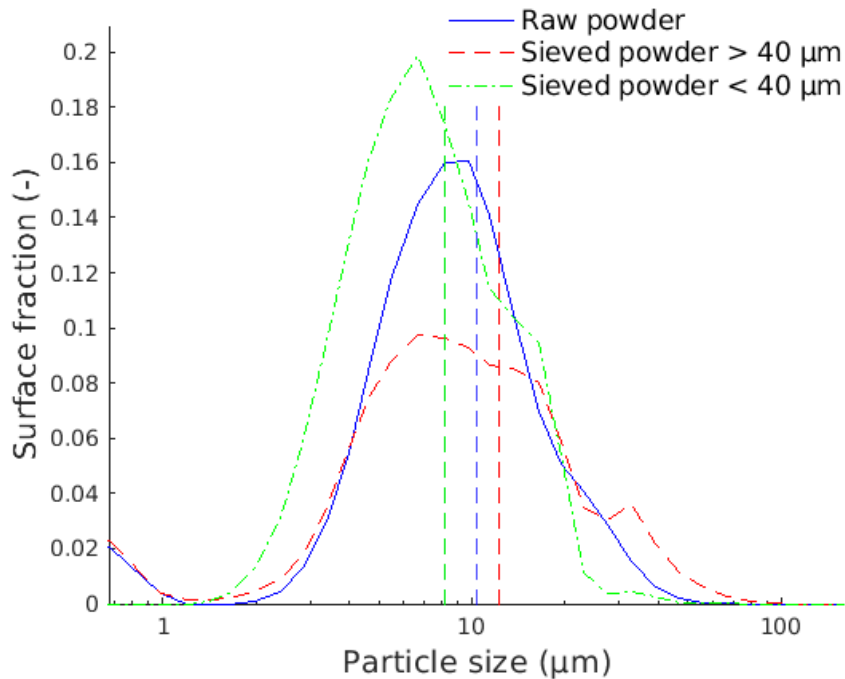
210 *Table 1. Characteristics of the raw and sieved nanocellulose*

Powder	Raw powder	Fine fraction	Large fraction
Sieving size (μm)	N/A	< 40	> 40
Mean surface diameter by sedimentation (μm)	48	10	54
Mean surface diameter 60 ms after dispersion in the 20 L sphere (μm)	10	8	12

211

212 The dust clouds produced after dispersion in the 20 L sphere were also characterized at the
 213 moment of ignition, i.e. 60 ms after the dust injection (Table 1). First, it can be confirmed that
 214 the injection system tends to break the powder agglomerates, as already shown by previous
 215 studies (Du et al., 2015; Sanchirico et al., 2015). Despite the high shear stress induced by the
 216 dispersion system of the 20 L sphere, a slight difference in the particle size distributions of the
 217 samples can be observed in Figure 3. Indeed, the mean surface diameter obtained by
 218 dispersion of the powder sieved below 40 μm is 8 μm whereas the dispersion of the bigger
 219 agglomerates (> 40 μm) led to a mean surface diameter of 12 μm . As a comparison, the mean
 220 surface diameter by dispersion of the raw powder is 10 μm , which confirms the efficiency of
 221 the sieving procedure.

222



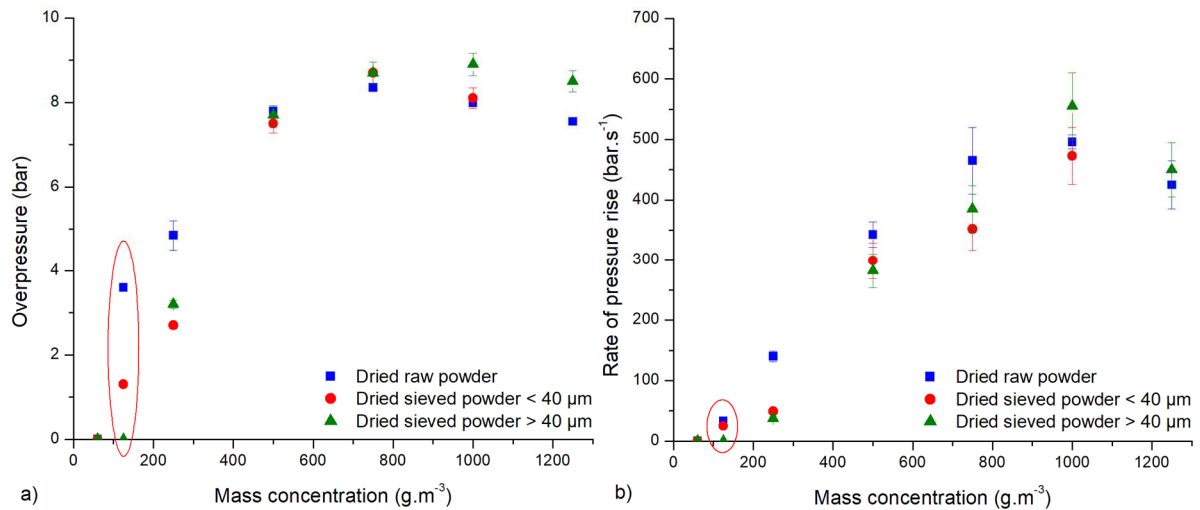
223

224 *Figure 3. Particle size distribution of raw and sieved nanocellulose after injection in the 20 L*
 225 *at the place and moment of ignition (60 ms after dispersion) measured by the Helos*
 226 *diffraction sensor (R3 lens, 0.5 – 175 μm)*

227

228 The explosion tests performed on the different samples conducted to rather similar explosion
 229 severities, probably due to the small differences in the PSD after dispersion. Indeed, a
 230 maximum overpressure of 8.9 ± 0.4 bar and a maximum rate of pressure rise of 555 ± 66
 231 $\text{bar}\cdot\text{s}^{-1}$ were obtained for the bigger agglomerates ($> 40 \mu\text{m}$) whereas these values respectively
 232 reached 8.7 ± 0.4 bar and $473 \pm 56 \text{bar}\cdot\text{s}^{-1}$ for the finest powder (Figure 4), which does not
 233 constitute a significant difference with regard to the experimental uncertainties. Nevertheless,
 234 the lowest concentration inducing an explosion was obtained at $125 \text{g}\cdot\text{m}^{-3}$ with the raw
 235 powder and the smallest agglomerates and only at $250 \text{g}\cdot\text{m}^{-3}$ with the sample of agglomerates
 236 bigger than $40 \mu\text{m}$. Thus, despite the breakage of the majority of the agglomerates observed in
 237 Figure 3, the sample constituted of agglomerates bigger than $40 \mu\text{m}$, which contains fewer
 238 fine particles than the initial powder, appears to be less ignition sensitive than the two other

239 samples. This observation tends to corroborate the theory stipulating that the ignition
240 sensitivity of a powder is mainly affected by the presence of fine particles (Saeed et al., 2019)
241 as they are more prone to volatilize.



242 a) b)

243 *Figure 4. Effects of nanocellulose sieving on a) the maximum overpressure and b) the*
244 *maximum rate of pressure rise*

245
246 To further investigate on the influence of fine particles on the ignition sensitivity, ignition
247 energy tests were conducted in the modified Hartmann tube. The minimum ignition energy of
248 the raw dried powder was evaluated at 5 mJ. After drying and sieving at 40 μm , both obtained
249 fractions also presented minimum ignition energies of 5 mJ. As their MIE is lower than
250 10 mJ, these powders can be considered as being very sensitive to electrostatic ignition (Janès
251 et al., 2008). However, when drying and sieving at 70 μm , the bigger fraction exhibited a
252 minimum ignition energy of 14 mJ. It should be noted that the MIE of microcrystalline
253 cellulose (MCC) ranges from 30 to 100 mJ for 30 μm particles (BGIA, 1997) and previous
254 tests performed on MCC with a mean diameter of 100 μm led to a MIE of 590 mJ .
255 These tests highlight the effects of the presence of fine particles on the ignition sensitivity,
256 especially for nanomaterials comprised of various sizes of agglomerates. Nevertheless,

257 sieving is probably not the most accurate method of powder selection, as small particles can
258 stick to agglomerates (due to electrostatic interactions, for instance) and remain in the upper
259 fraction, although smaller than the mesh. Furthermore, for non-spherical particles, only one
260 dimension smaller than the mesh is sufficient for an agglomerate to be retrieved in the low
261 fraction, independently from its volume. As a consequence, in order to stress the influence of
262 agglomeration of nanopowders on their explosion severity and MIE, the impact of mechanical
263 agglomeration has been studied.

264

265 **3.2. Effects of mechanical agglomeration: example of carbon coated silicon**

266 Since the agglomerates that naturally exist in the raw powder (especially for nanocellulose)
267 are easily breakable and in order to assess the influence of the particle size distribution on the
268 explosion severity, the effects of mechanical agglomeration were investigated through carbon
269 coated silicon (Si Ω C). The initial mean surface diameter was measured by sedimentation of
270 the powder using the laser diffraction sensor (Helos – Sympatec) and by wet dispersion in
271 ethanol using a Mastersizer 2000 S (Malvern Instruments). Analyzing the wet dispersion
272 measurements presented in Table 2, it appears that all the agglomerated samples present a
273 mean diameter much higher than that of the raw powder, i.e. 68 μm , and that the powder B
274 exhibits the highest diameter, reaching 442 μm , which is consistent with the SEM
275 observations. However, when regarding the powders agglomerated by process A, it seems that
276 the powder A1 (260 g.L^{-1}) is more agglomerated than the powder A2 (400 g.L^{-1}), which seems
277 inconsistent with SEM observations. Once again, it should be kept in mind that the wet
278 dispersion in ethanol modifies the interactions between particles (variation of zeta potential)
279 and does not provide accurate information concerning the particle size distribution of a
280 powder in air.

281 The surface diameter was measured by sedimentation of the powder using two lenses of the
 282 laser diffraction sensor: R3 and R5 (Table 2). Tests performed with the R3 lens led to rather
 283 similar mean surface diameters by sedimentation, from 20 μm to 32 μm , which can be due to
 284 the upper limitation of the lens. The R5 lens allows the measurement of particles from 4.5 to
 285 875 μm , inducing that the agglomerates observed by SEM can be distinctly observed. First,
 286 the powder B is then confirmed to be the most agglomerated ($d_{50,R5} = 297 \mu\text{m}$), although this
 287 was not visible using the R3 lens. Then, the sample A2 presents a lower mean diameter than
 288 the sample A1, which is conversely proportional to the particle density and confirms the
 289 measurements performed by wet dispersion. Finally, the raw powder presents a mean surface
 290 diameter of 207 μm , which is considerably higher than the size of the agglomerates observed
 291 by SEM. It should be reminded that this lens does not allow the measurement of particles
 292 smaller than 4.5 μm , implying that the small agglomerates may not be measured by the
 293 apparatus.

294

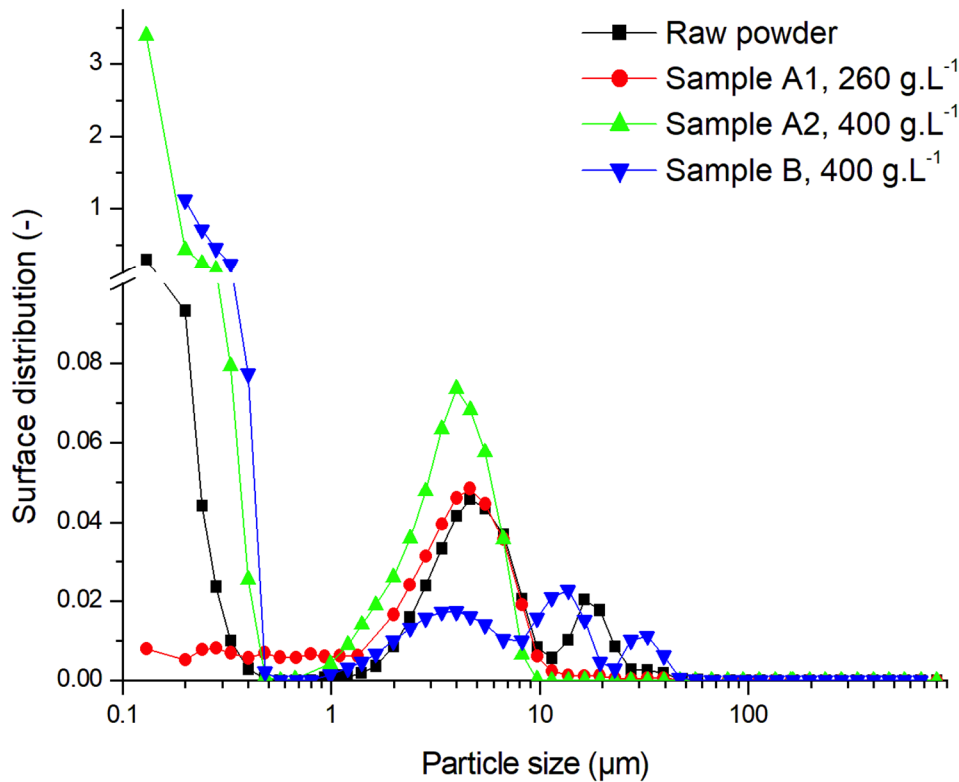
295 *Table 2. Mean diameter of the different samples of carbon-coated silicon measured by*
 296 *sedimentation and wet and dry dispersion*

	Raw powder	Sample A1	Sample A2	Sample B
Mean diameter by wet dispersion in ethanol (μm) – Mastersizer 2000 S	68	352	261	442
Mean surface diameter by sedimentation – R5 lens (μm) – Helos laser diffraction sensor	207	249	132	297
Mean surface diameter by sedimentation – R3 lens (μm) – Helos diffraction sensor	30	26	32	20
Mean surface diameter after dispersion in the 20 L sphere – R1+R3+R5 Helos diffraction sensor	9	4	3.5	12

Mean surface diameter after dispersion in the Scirocco device (μm) – Mastersizer 2000	3.5	5.3	5	20
--	-----	-----	---	----

297

298 To estimate the PSD during the combustion and specifically at the moment of ignition,
 299 dispersion tests were performed with the laser diffraction sensor coupled with the
 300 visualization 20 L sphere. Nevertheless, as seen in Table 2, each lens gives a peculiar and
 301 useful information on the PSD, but in the case of a nanopowder, a more global view is
 302 necessary. Unfortunately, as previously said, no apparatus currently allow such a
 303 measurement (from nm to hundreds of micrometers) at high frequency and concentration. An
 304 alternative solution could consist in using the same in-situ laser sensor and repeating three
 305 times (at least) the same dust dispersion experiment with the three lenses (R1, R3 and R5). In
 306 order to normalize the intensities of the peaks, it may be useful to insert an internal reference
 307 (nearly monomodal powder of low and fixed concentration, with a narrow PSD which does
 308 not interfere with the studied powder). An instance of such application for carbon-coated
 309 silicon is given in Figure 5.



310

311 *Figure 5. Representation of the global PSD of carbon-coated silicon powders after dispersion*
 312 *in the 20 L ($t_v = 60$ ms) obtained by the concatenation of PSD measurements done with R1,*
 313 *R3 and R5 (Helos – Sympatec)*

314

315 Figure 5 allows the visualization of the PSD of the nanopowders over a wide range of sizes
 316 (from 0.1 μm to 875 μm). It appears that sample B (400 g.L^{-1}) presents the biggest
 317 agglomerates after dispersion in the sphere, with modes at 4, 15 and 35 μm (omitting the
 318 primary particles and nanometric agglomerates). The powders A1 and A2 show the smallest
 319 agglomerates after dispersion, with mean surface diameters of 4 and 3.5 μm , respectively
 320 (Table 2). The raw Si Ω C powder, in addition to the common agglomeration mode at
 321 approximately 4 μm , also presents larger structures around 20 μm (Figure 5). It should be
 322 noticed that, unlike the other samples, no significant peak is obtained for the powder A1 at

323 particle size lower than 0.5 μm which may seem surprising and requires additional tests with
324 R1 lens.

325 These observations can lead to several comments: i) The measuring range being limited at
326 0.1/0.2 μm , the particle size distributions may be different below this value, and the presence
327 of individualized nanoparticles is certainly more marked for the raw powder. ii) The dust
328 injection in the 20 L sphere clearly induces the fragmentation of the biggest structures (Table
329 2); however, the process B seems to generate more cohesive agglomerates over a wider range
330 of particle sizes. iii) During the agglomeration process, especially with the process A, the
331 structure of the initial agglomerates could have been weakened, reducing the cohesion
332 strength of these initial agglomerates. During particle size measurements by wet dispersion or
333 by sedimentation in air, their structure is not significantly modified. On the contrary, the very
334 high shear rate induced by the dispersion in the 20 L sphere (pressurization at 20 bar) can
335 break these agglomerates, demonstrating the existence of a threshold stress.

336

337 Table 2 and Figure 5 demonstrate the fragmentation of agglomerated structures during the
338 injection of Si Ω C in the 20 L sphere, but quantitative indicators can be proposed. For
339 instance, a diameter variation, defined by $\Delta D = 100 \cdot \frac{(d_{\text{agg}} - d_{50})}{d_{\text{agg}}}$ was calculated by Sanchirico
340 et al. (2015), who classified the powders into two classes: class 1 containing the hardest dusts
341 ($\Delta D < 50\%$) and class 2 for powders that undergo greater breakage ($\Delta D > 50\%$). By
342 considering only the smaller agglomerates (lens R3), values between 75 % and 98 % were
343 obtained in this work, implying that all the powders are in class 2. It should be underlined that
344 those values are slightly higher than that presented by Sanchirico et al. (2015). Nevertheless,
345 these authors collected the dust several minutes after dust settling, which potentially allows

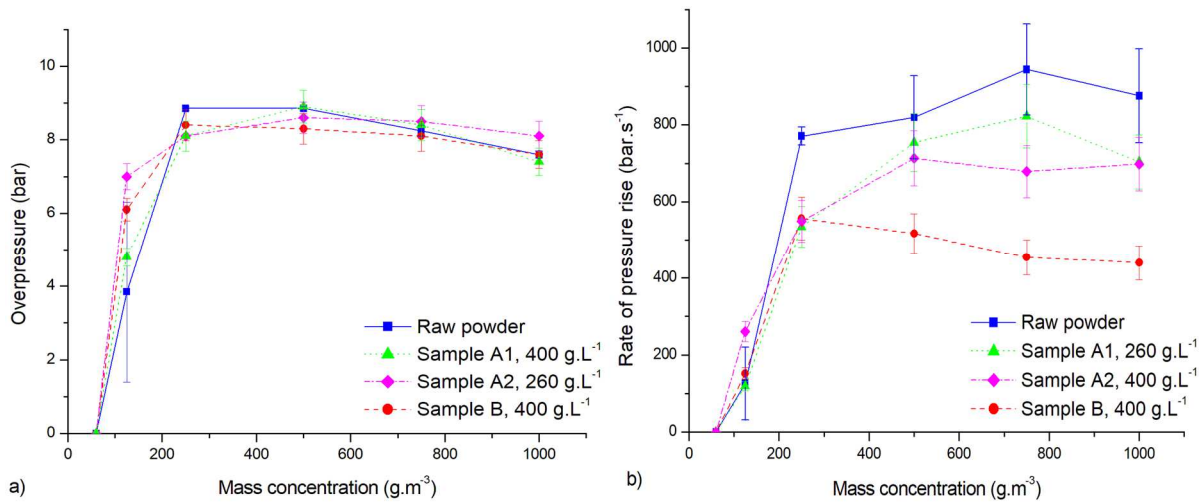
346 the re-agglomeration of the powder, whereas the measurements in this work were conducted
347 directly within the sphere and correspond to the moment and place of ignition.

348 Dry PSD measurements were also conducted using the Mastersizer 2000 particle size analyzer
349 equipped with a dispersion system called Scirocco (Malvern Instruments). This apparatus
350 allows the measurement of particle sizes from 0.2 to 2000 μm . The powder dispersion is
351 ensured before the measurement by an air jet in a Venturi configuration (Ali et al., 2015;
352 Bonakdar et al., 2016). Although this measurement is not conducted at the same conditions as
353 the explosion tests, the evaluation of the particle size distribution after dispersion of the
354 powder still provides information on the potential agglomerate breakage during the
355 dispersion. The results, also presented in Table 2, are consistent with the SEM images, as the
356 powder B seems the more agglomerated, with a mean surface diameter of 20 μm , whereas the
357 raw powder presents the smallest particles and a mean surface of 3.5 μm . It should be noted
358 that the shear stress induced by the dispersion in the Scirocco device is much lower than that
359 induced during the injection in the 20 L sphere, notably due to a lower dispersion pressure (2
360 barg). Such values tend to show that most of the initial agglomerates are broken during the
361 dispersion in the 20 L sphere, but not necessarily in the Scirocco device, which corroborates
362 that the agglomerates fragmentation depends on the application of a threshold stress.
363 However, a whole characterization of the particle size distribution, from the nanometer to
364 several hundred of micrometers and for both apparatuses, is necessary to conclude on this
365 phenomenon.

366

367 Explosion tests were performed on each sample in the standard 20 L sphere (Figure 6). First,
368 it should be noticed that the increase of overpressure and rate of pressure rise with the dust
369 concentration is very fast, which tends to decrease the accuracy at the ‘transition’
370 concentration, i.e. 125 $\text{g}\cdot\text{m}^{-3}$. Indeed, in this transition zone, a small variation in the dust

371 concentration can greatly impact the pressure-time evolution. The maximum overpressures
 372 obtained are similar independently of the agglomeration state of the sample, reaching around
 373 8.8 bar (Figure 6a), which implies that the same amount of powder seems to react. From the
 374 observation of the overpressure evolution with the concentration, agglomeration seems to
 375 have a limited effect on the thermodynamic development of the explosion. On the other hand,
 376 significant differences appear when regarding the maximum rate of pressure rise obtained for
 377 each powder (Figure 6b). The raw powder leads to the most severe explosion, with a
 378 maximum rate of pressure of $944 \pm 118 \text{ bar}\cdot\text{s}^{-1}$. The less agglomerated (at least theoretically)
 379 powder i.e. SiQC A1, is slightly less severe and reaches $822 \pm 98 \text{ bar}\cdot\text{s}^{-1}$. Both powders are
 380 then classified in the St2 class, with explosivity index K_{St} of respectively $256 \pm 32 \text{ bar}\cdot\text{m}\cdot\text{s}^{-1}$
 381 and $223 \pm 27 \text{ bar}\cdot\text{m}\cdot\text{s}^{-1}$. The explosions produced by the powders agglomerated with a density
 382 of $400 \text{ g}\cdot\text{L}^{-1}$ are less severe, reaching $713 \pm 85 \text{ bar}\cdot\text{s}^{-1}$ for the sample A2 and only 556 ± 60
 383 $\text{bar}\cdot\text{s}^{-1}$ for the sample B, which ranks both powders as St1.



385 *Figure 6. Evolution of the a) maximum overpressure and b) maximum rate of pressure rise as*
 386 *a function of the mass concentration of the four samples of carbon-coated silicon*

387

388 Then, it appears that only the maximum rate of pressure rise is affected by the agglomeration
389 state of the powder. Considering spherical particles, the density of each powder and the mean
390 surface diameter measured after dispersion in the 20 L sphere (Table 2), the reactive surface
391 area developed after dispersion was calculated for each sample at each concentration.
392 Contrary to the obvious correlations between the explosion severity and the reactive surface
393 observed for starch powders (Santandrea et al., 2019a), no clear relationship could be
394 extracted for the carbon coated silicon. Indeed, if the combustion of organic powder is limited
395 by the pyrolysis step or by the surface reaction of the particles (Di Benedetto et al., 2010), the
396 carbon-coated silicon does not undergo such pyrolysis step. Since the combustion does not
397 occur in gaseous phase, the distance between the particles is of great importance. Indeed,
398 increasing the concentration in the same volume reduces this distance, possibly leading to a
399 transition between the combustion of the individual particle (small concentration) to a group
400 combustion at higher concentrations. On the contrary, promoting the agglomeration tends
401 both to increase the average distance between the combustible structures and to decrease the
402 surface concentration.

403 After each explosion test, the evolution of the pressure was recorded during the cooling phase.
404 Since the combustion of silicon consumes oxygen and produces silica, the final pressure in the
405 sphere is lower than the atmospheric pressure, even if the combustion of the carbon layer
406 leads to the production of, among others, carbon monoxide and carbon dioxide. The stabilized
407 pressure after explosion can provide information on the combustion gases production and
408 oxygen consumption (Figure 7).

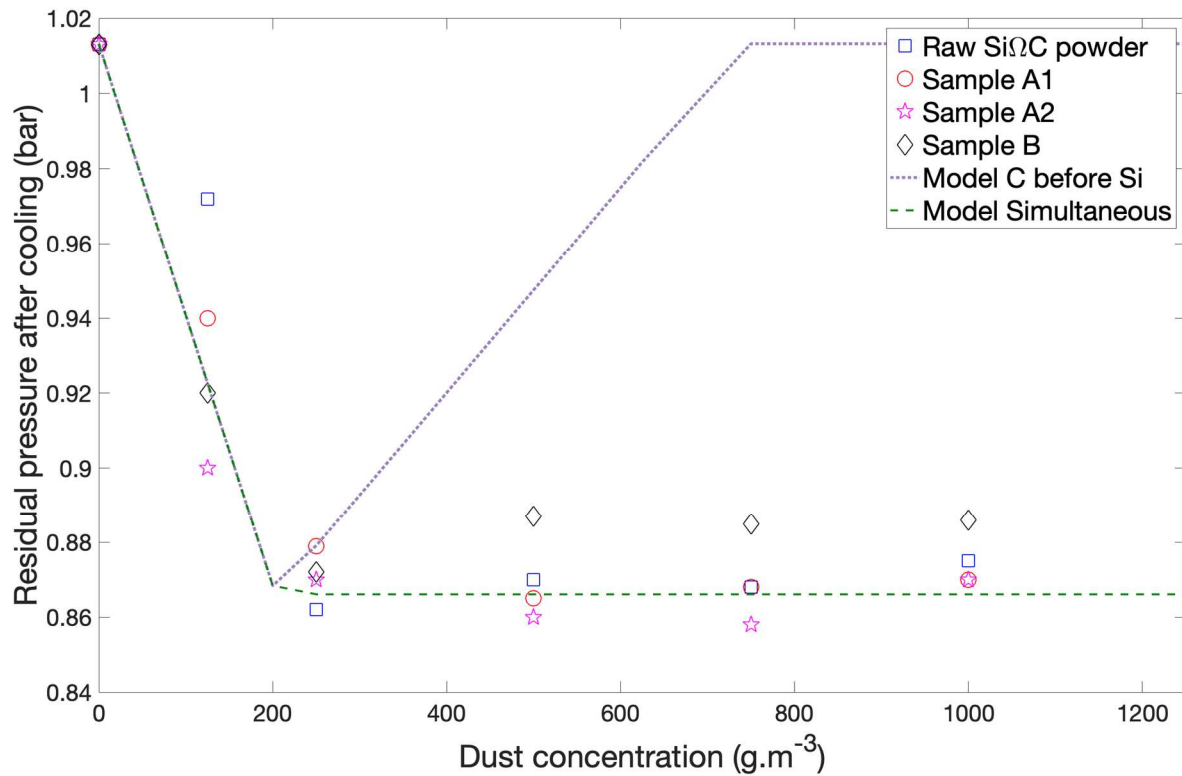
409 To evaluate the combustion mechanisms, two hypotheses were investigated. First, successive
410 reactions were considered: the carbon C reacts first, followed by the silicon Si (Figure 7). The
411 second hypothesis consists of simultaneous reactions of the carbon and the silicon, the oxygen
412 consumption by each reaction being proportional to the molar proportions of C and Si. The

413 considered reactions are the formation of carbon dioxide from the carbon and oxygen, and the
414 reaction of silicon with oxygen to form silica (SiO_2). Assuming that the particle diameter is
415 40 nm with 2 nm of carbon coating, a molar proportion of 27.4% of carbon and 72.6% of
416 silicon was considered. In light of the similar measured overpressures, it was previously
417 established that the reaction products were not significantly affected by the agglomeration
418 state. For a given mass concentration, the same amount of powder is then assumed to be
419 consumed for each sample and the reaction of nitrogen with silicon was neglected.

420 It appears in Figure 7 that the experimental residual pressure seems to follow the same
421 evolution than in the case of simultaneous reactions of carbon and silicon, even if the carbon
422 layer is the first compound theoretically in contact with oxygen. Such behavior can notably be
423 explained by the combustion of silicon in vapor phase, which is confirmed by considering
424 Glassman's criterion: the boiling point of Si (2355°C) is much lower than the volatilization
425 temperature of its oxide (2950°C for silica) or of its carbon layer (more than 4000°C). As a
426 consequence, after ignition, i.e. at high temperatures, the carbon coating does not prevent or
427 hinder the combustion of the silicon. If the second model seems to represent satisfactorily the
428 experimental data, a concentration shift is visible for the low dust concentrations. Indeed, the
429 value experimentally measured at 125 g.m^{-3} for the raw powder, i.e. around 0.97 bara,
430 corresponds to the value calculated at 60 g.m^{-3} by both models. As a lower pressure would
431 have been theoretically expected, this shift may be due to oxygen adsorbed onto the particles
432 surface, reacting more easily with the carbon layer and generating an extra amount of carbon
433 dioxide. Moreover, Figure 7 shows that the powders agglomerated by the process A, i.e.
434 powders A1 and A2, follows globally the same evolution than the raw powder with a final
435 pressure stabilized around 0.87 bara. On the contrary, the final pressure obtained after
436 combustion of powder B stabilized around 0.89 bara, which confirms the specificity of this
437 powder due to the agglomeration process. Due to the PSD of sample B being greater than

438 those of the other Si Ω C powders, the heating rate of such structures is probably slower, which
439 may modify the reaction mechanism, promoting the effect of the carbon layer and thus
440 leading to a lowest explosion severity.

441



443

444 *Figure 7. Evolution of the stabilized pressure after explosion in the 20 L sphere with the mass*
 445 *concentration: experimental data for the different samples of carbon-coated silicon and*
 446 *models for the raw powder*

447

448 In addition to the experiments conducted in the 20 L sphere, the minimum ignition energy
 449 (MIE) of the different powders was determined in the modified Hartmann tube according to
 450 ISO/IEC 80079-20-2 (2016). While the MIE of the raw powder was evaluated at 5 mJ, no
 451 ignition was observed at 1J for the three other samples when varying the dust quantity from
 452 0.6 to 1.8 g and the ignition delay time from 90 ms to 150 ms. Although some glowing
 453 particles were observed when testing the sample A1, no flame was obtained. The
 454 agglomeration then appears to significantly reduce the ignition sensitivity of SiΩC powders,
 455 turning very sensitive raw powders to samples almost insensitive to electrostatic ignition

456 (Janès et al., 2008). By examining the evolution of the PSD in the tube with the R5 lens, it
457 appears that mean surface diameters of 82 and 252 μm were obtained for raw Si Ω C sample
458 and sample B, respectively; which is consistent with MIE results.

459 Nevertheless, as shown in Figure 6, the lowest concentration for which an explosion was
460 obtained at 10 kJ is the same for all the samples, i.e. 125 $\text{g}\cdot\text{m}^{-3}$. Since these tests were
461 performed at 10 kJ, additional tests should be conducted with the standard ignition energy to
462 apply to determine the LEL, i.e. 2 kJ (EN 14034-3, 2006). Still, the LEL does not seem
463 significantly modified by the agglomeration state of the powder, which can notably be
464 explained by the strong fragmentation of the agglomerates during the dispersion in the 20 L
465 sphere. Indeed, the agglomerates submitted to the high shear stress of the injection device in
466 the 20 L sphere tend to break more easily than the agglomerates lifted by the air pulse in the
467 modified Hartmann tube, which give them ignition properties similar than the raw powder.
468 This point will be developed in the next section.

469

470 **3.3. Some theoretical clues on relating the dispersion process and the particle size** 471 **distribution of nanopowders clouds**

472 Inertia, rotary and turbulent stresses are the three main stresses exerted by the fluid flow on
473 the particles surface. It seems important to consider them as their evolution can explain the
474 deagglomeration phenomenon and thus, the changes in the ignition sensitivity and explosivity
475 previously described.

476 The inertia stress is due to agglomerates shifts and accelerations in the flow direction. It can
477 be defined by equation 1 (Deng et al., 2016; Weiler et al., 2010):

$$478 \sigma_l = \frac{\rho}{8} \cdot \left[1 - \frac{\arccos\left(\frac{d_p}{d_{agg} - d_p}\right)}{180^\circ} \right] \cdot (u_p - u)^2 \cdot \left[\frac{24}{\text{Re}_{rel}} + \frac{24}{\text{Re}_{rel}^{0.5}} + 0.4 \right] \quad (1)$$

479 where ρ is the fluid density; d_p , its primary diameter; d_{agg} , the diameter of the agglomerate; u ,
 480 the flow velocity; u_p , the agglomerate velocity and Re_{rel} , the Reynolds number calculated
 481 from the slip velocity u_s between the agglomerates and the gas:

$$482 \quad u_s = (u_p - u) = d_p^2 \frac{(\rho_p - \rho)}{18\mu} \cdot a \quad (2)$$

483 where ρ_p is the particle density; μ the fluid dynamic viscosity and a the acceleration term.

484 The rotary stress σ_r is generated in zones with high velocity gradient (du/dz). Weiler et al.
 485 (2010) defines it as follows:

$$486 \quad \sigma_r = \frac{\rho_p}{40} \cdot (d_{agg})^2 \cdot \left(\frac{du}{dz}\right)^2 \quad (3)$$

487 Finally, turbulent stresses σ_T caused by the vortices present in the velocity field can also lead
 488 to agglomerate breakage both due to impaction between solid structures and to shear stresses.
 489 They depend on the ratio between the Kolmogorov scale and the agglomerate size and are
 490 expressed as a function of fitting parameters a_i given by Weiler et al. (2010):

$$491 \quad \sigma_T = a_1 \rho \cdot \left[\frac{v_{kin}^{(3a_2-1)}}{l_D^{4 \cdot a_2}} \right]^{a_3} \cdot (d_{agg})^{a_4} \quad (4)$$

492 where v_{kin} is the kinematic viscosity of the fluid and l_D , the Kolmogorov scale of the flow.
 493 The latter parameter can be found for the 20 L sphere at various dispersion times, especially at
 494 10, 50 and 100 ms for Kolmogorov scale (Dahoe et al., 2001; Ogle, 2016). Due to l_D values
 495 being unavailable for dust dispersions in the Hartmann tube, they have been evaluated by the
 496 following equation:

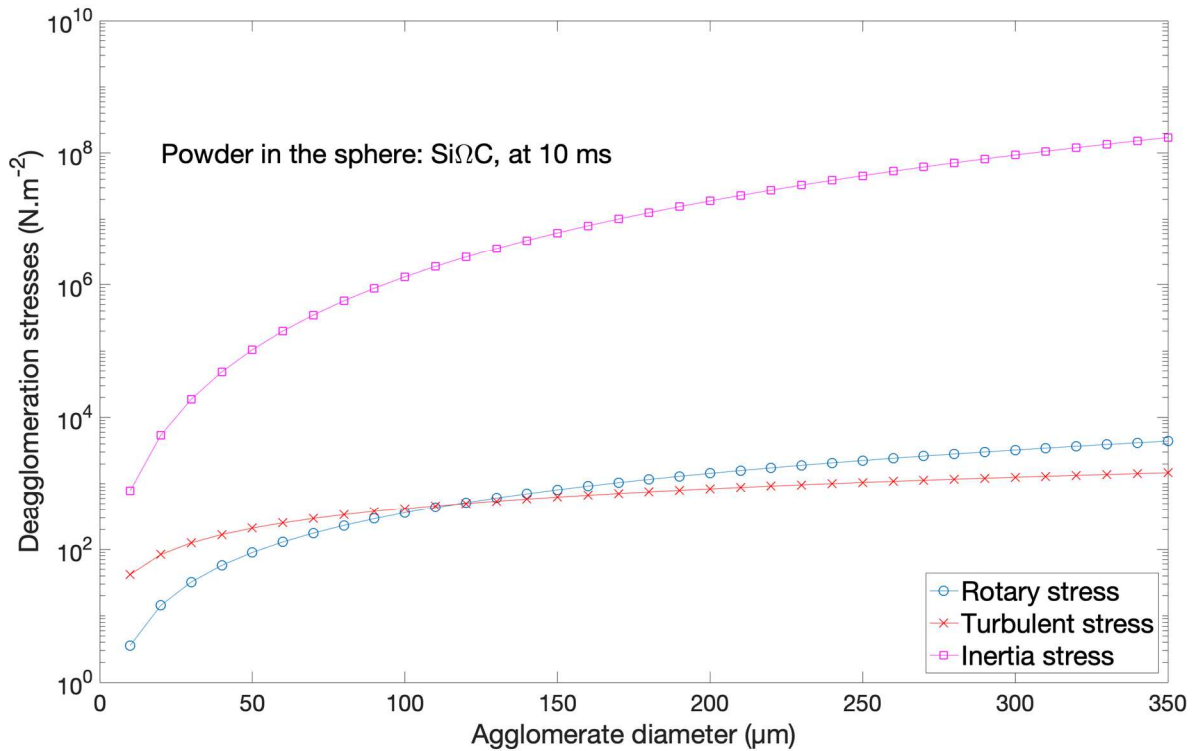
$$497 \quad l_D = \left(\frac{v_{kin}^3}{\varepsilon} \right)^{0.25} \quad (5)$$

498 where ε is the turbulence dissipation rate which can be estimated as follows by considering
 499 only the vertical direction z :

$$500 \quad \varepsilon = 15 \cdot v_{kin} \cdot \left(\frac{du_z}{dz}\right)^2 \quad (6)$$

501 This assumption made on a privileged direction of the particle flow is confirmed by previous
502 Particle Image Velocimetry (PIV) experiments (Cuervo, 2015). Particles and agglomerates
503 velocities, velocity gradients and acceleration were determined both for the sphere and the
504 tube by CFD simulations and were validated experimentally by PIV measurements (Cuervo,
505 2015; Murillo, 2016).

506 Figure 8 shows that the inertia stress is by far the greatest stress which applies on the
507 agglomerates, significantly increasing when d_{agg} increases. The predominance of drag forces
508 on other fragmentation mechanisms is confirmed by other authors (Breuer and Khalifa, 2019)
509 and is illustrated by a Stokes number greater than 90 for a dust dispersion of Si Ω C in the
510 sphere, corresponding to large relative velocities between the agglomerates and the flow.
511 However, other mechanisms such as the impaction of large particles on the upper and lower
512 plates of the rebound nozzle (Kalejaiye et al., 2010) should not be neglected. It should be
513 stressed that the calculations were performed for the first 10 ms of the dust dispersion as high
514 acceleration rates specifically occur on short time scales (Murillo, 2016; Weiler et al., 2010).



515

516 *Figure 8. Evaluation of the intensities of the rotary, turbulent and inertia stresses in the 20 L*
517 *sphere for Si Ω C agglomerates*

518

519 Figure 9 represents the evolution of the global stress (sum of inertia, rotary and turbulent
520 stresses) exerted on Si Ω C agglomerates both in the 20 L sphere and in the modified Hartmann
521 tube. At first, it can be noticed that, whatever the dispersion time, the stress which applied on
522 the agglomerates in the 20 L sphere is always greater than in the modified Hartmann tube. It
523 can explain why the agglomerated samples of Si Ω C showed a minimum ignition energy
524 greater than 1 J as they cannot be fragmented during their dispersion in the tube. On the
525 contrary, Figure 5 demonstrates that the Si Ω C samples can be deagglomerated, at least
526 partially, by their injection in the 20 L vessel. As previously said, Figure 9 also confirms that
527 the fragmentation occurs during the first moments of the dust dispersion, when the
528 acceleration and the slip velocity are the greatest. Three models were used to assess the
529 agglomerate strength σ_{agg} and compare it to the deagglomeration stress (Kendall, 1988;
530 Rumpf, 1962; Weiler et al., 2010). Rumpf model assumes that the agglomerate is separated in
531 two parts by a transverse section, without taking into account the actual structure of the
532 agglomerate. It implies that the breakage occurs through a simultaneous rupture of all the
533 bonds along the fracture plan:

534
$$\sigma_{agg,R} = \frac{9}{8} \cdot \left(\frac{1-\epsilon_p}{\epsilon_p} \right) \cdot \frac{F_c}{d_p^2} \quad (7)$$

535 where ϵ_p is the porosity of the agglomerate and F_c , the cohesion force, limited here to the Van
536 der Waals forces F_{vdw} . With regard to the work presented by Deng et al. (2016), the porosity
537 of Si Ω C agglomerates was set at 0.8 and F_{vdw} was estimated through the following
538 relationship valid for 2 identical spheres:

539
$$|F_{vdw}| = \frac{H \cdot d_p}{24 \cdot h_p^2} \quad (8)$$

540 where H is the Hamaker constant and h_p is the cutoff of separation, set at 0.165 nm (Deng et
 541 al., 2016). As Si is coated by a carbon layer, an average Hamaker constant H of $2.5 \cdot 10^{-19}$ J
 542 was chosen, based on the work of Dagastine et al. (2002), indicating that this value is valid for
 543 graphite particles in air.

544 Kendall (1988) claimed that a more gradual rupture occurs and that the real cohesion strength
 545 of an agglomerate is overestimated by Rumpf model. As a consequence, the following
 546 relation was proposed for the cohesion strength:

$$547 \quad \sigma_{\text{agg,K}} = 15.6 \frac{(1-\varepsilon_p)^4}{d_p} \cdot \frac{H}{12 \cdot \pi \cdot h_p^2} \quad (9)$$

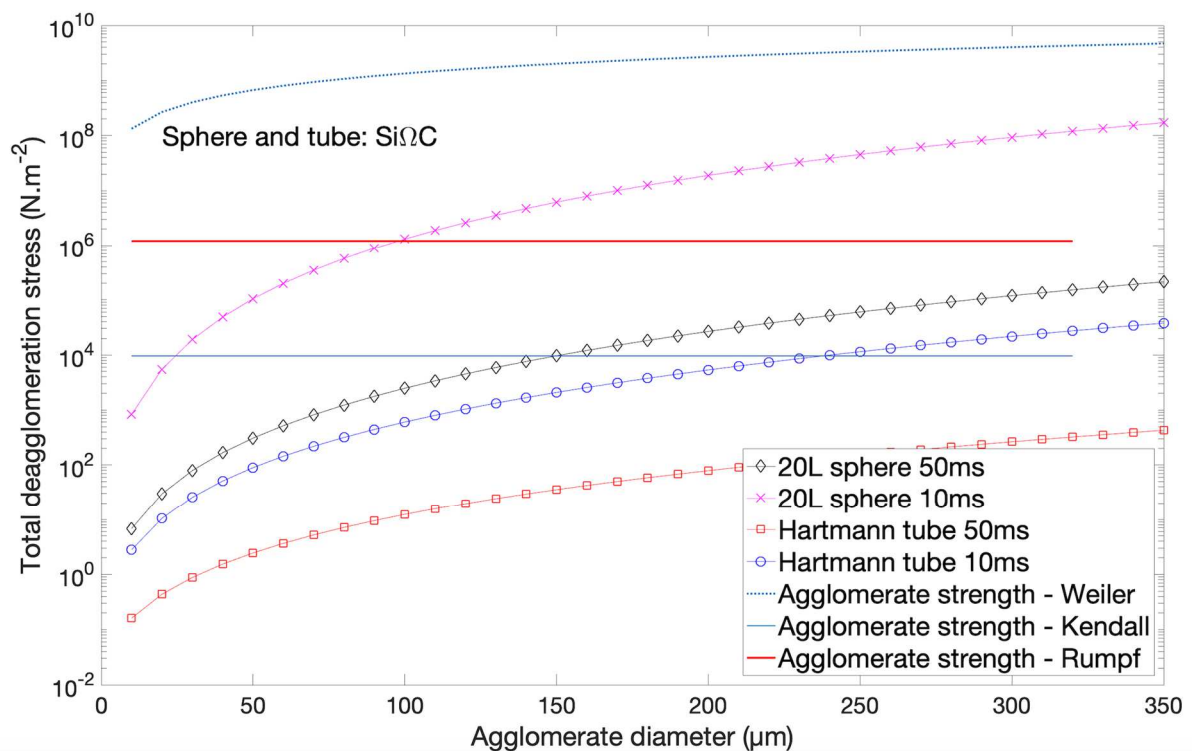
548 Finally, Weiler et al. (2010) proposed an alternative model assuming a total breakage of the
 549 agglomerates, by considering all the contacts between the particles. Obviously, the cohesion
 550 strength of such structure is greater than those obtained by the previous models:

$$551 \quad \sigma_{\text{agg,W}} = \frac{(1-\varepsilon_p)}{\varepsilon_p} \cdot \frac{F_c}{2 \cdot d_{\text{agg}}^2} \cdot \left[\left(\frac{d_{\text{agg}}}{d_p} \right)^3 - \frac{4 \cdot \left(1 - \frac{\text{Arccos}(b)}{180^\circ} \right)}{b^2} \right] \quad (10)$$

$$552 \quad \text{with } b = \frac{d_p}{d_{\text{agg}} - d_p}.$$

553 In Figure 9, it should be noticed that, even in the 20 L sphere, the stresses are not sufficient to
 554 break every Van der Waals bond of Si Ω C agglomerates, which is notably confirmed by
 555 Figure 5 in which microstructures are still clearly visible. By applying Rumpf model, it seems
 556 that only the structures larger than 90 μm will be broken during a dust injection in the 20 L
 557 sphere, whereas the limit defined by Kendall model is close to 25 μm . The latter value is
 558 consistent with the measurements performed with the laser sensor (Figure 5), but no larger
 559 agglomerates are visible after dust dispersion in the sphere, which tends to support Kendall's
 560 approach. These conclusions are also in accordance with the Monte Carlo simulations
 561 developed by Deng et al. (2016) on 50 nm primary particles. Indeed, they obtained cohesion
 562 strengths of $2.8 \cdot 10^4$ Pa and $1.7 \cdot 10^5$ Pa for Kendall and Rumpf models, respectively.

563 Nevertheless, it should be underlined that the cohesion strengths presented in our study should
 564 be considered as orders of magnitude as they are greatly dependent on variables which are
 565 difficult to quantify, such as Hamaker constant and the cutoff of separation. The same
 566 approach can be applied to nanocellulose dispersion, with similar conclusions. However, it
 567 will not be detailed here as the fibrous nature of the primary particles makes even more
 568 difficult to define their structural properties.



569
 570 *Figure 9. Evaluation of the intensities of the deagglomeration stresses in the 20 L sphere and*
 571 *in the modified Hartmann tube for SiΩC agglomerates. Comparison with cohesion strengths*
 572 *models.*

573

574 4. Conclusions

575 The ignition and explosion characteristics of nanocellulose and silicon coated by carbon were
 576 studied with regard to their agglomeration state, through sieving and mechanical
 577 agglomeration. It mainly appears that the agglomerates, naturally or intentionally generated,

578 can be broken if a sufficient stress is applied during their dispersion. The threshold stress can
579 be roughly estimated using models allowing for the determination of the cohesion strength of
580 agglomerates (Kendall model for instance).

581 When applying rather low shear stresses, as for instance during the dust dispersion in a
582 modified Hartmann tube, only the largest structures can be broken, and the minimum ignition
583 energy is greatly modified by the presence of big agglomerates. However, if a greater stress is
584 applied, such as during the dust dispersion in the 20 L sphere, most of the micrometric
585 agglomerates can be broken and the explosion severity is only slightly affected by the
586 presence of brittle agglomerates. But when harder structures are formed, as it is the case for
587 Si Ω C produced by the process B, the maximum rate of pressure rise is significantly decreased
588 and the combustion mechanisms can also be altered.

589 Such modification of the explosion risk may be considered as a direct application of the
590 moderation principle of inherent safety. By intentionally agglomerating nanopowders, their
591 ignition sensitivity, but also to a lesser extent, their explosion severity, can be greatly reduced.
592 Nevertheless, it should be underlined that such assertion mainly depends on the stress which
593 will be applied to disperse the powders, during explosion tests, but above all, during an
594 accident. It should be added that a similar approach can be applied to micron-size particles or
595 ultrafine particles.

596 The specificity of the nanopowders lies in their high specific surface area. But a dust cloud of
597 nanopowders (at concentrations greater than the minimum explosive concentration) is always
598 highly polydispersed and the whole particle size distribution has to be considered. Each part
599 of the cloud can 'play its own role': the primary nanoparticles influences greatly the ignition
600 step, the primary aggregates or agglomerates of a few micrometers play a significant role in
601 the radiative heat transfer and the bigger micrometric structures can be both considered as

602 flame stretching agents and ‘fuel reserves’. But if the cohesion strength of the agglomerates is
603 too high with regard to the dispersion stress, the explosion risk will be lowered.

604

605 **References**

606 Ali, M., Bonakdar, T., Ghadiri, M., Tinke, A., 2015. Particle Breakage in a Scirocco
607 Disperser. *Powder Technol.* 285, 138–145.

608 <https://doi.org/10.1016/j.powtec.2015.06.048>

609 BGIA (1997). Combustion and explosion characteristics of dusts. BIA-Report 13/97 and
610 Gestis Database, HVBG, Sankt Augustin, Germany.

611 Boilard, S.P., Amyotte, P.R., Khan, F.I., Dastidar, A.G., Eckhoff, R.K., 2013. Explosibility of
612 micron- and nano-size titanium powders. *J. Loss Prev. Process Ind.* 26, 1646–1654.

613 <https://doi.org/10.1016/j.jlp.2013.06.003>

614 Bonakdar, T., Ali, M., Dogbe, S., Ghadiri, M., Tinke, A., 2016. A method for grindability
615 testing using the Scirocco disperser. *Int. J. Pharm.* 501, 65–74.

616 <https://doi.org/10.1016/j.ijpharm.2016.01.052>

617 Bouillard, J., Vignes, A., Dufaud, O., Perrin, L., Thomas, D., 2010. Ignition and explosion
618 risks of nanopowders. *J. Haz. Mater.* 181, 873–880.

619 <https://doi.org/10.1016/j.jhazmat.2010.05.094>

620 Breuer, M., Khalifa, A., 2019. Revisiting and improving models for the breakup of compact
621 dry powder agglomerates in turbulent flows within Eulerian–Lagrangian simulations.

622 *Powder Technol.* 348, 105–125. <https://doi.org/10.1016/j.powtec.2019.03.009>

623 Cuervo, N. 2015. Influences of turbulence and combustion regimes on explosions of gas- dust
624 hybrid mixture. Université de Lorraine (in English).

625 Dagastine, R.R., Prieve, D.C., White, L.R., 2002. Calculations of van der Waals Forces in 2-
626 Dimensionally Anisotropic Materials and Its Application to Carbon Black. *J.*
627 *Colloid Interface Sci.* 249, 78-83.

628 Dahoe, A.E., Cant, R.S., Scarlett, B. On the decay of turbulence in the 20-liter explosion
629 sphere (2001) *Flow, Turbul. Combust.* 67 (3), 159-184. doi:
630 10.1023/A:1015099110942.

631 Debrincat, D.P., Solnordal, C.B., Van Deventer, J.S.J., 2008. Characterisation of inter-particle
632 forces within agglomerated metallurgical powders. *Powder Technol.* 182, 388–397.
633 <https://doi.org/10.1016/j.powtec.2007.07.001>

634 Deng, X., Huang, Z., Wang, W., Davé, R.N., 2016. Investigation of nanoparticle
635 agglomerates properties using Monte Carlo simulations. *Adv. Powder Technol.* 27,
636 1971–1979. <https://doi.org/10.1016/j.appt.2016.06.029>

637 Di Benedetto, A., Russo, P., Amyotte, P., Marchand, N., 2010. Modelling the effect of
638 particle size on dust explosions. *Chem? Eng. Sci.* 65, 772–779.
639 <https://doi.org/10.1016/j.ces.2009.09.029>

640 Du, B., Huang, W., Liu, L., Zhang, T., Li, H., Ren, Y., Wang, H., 2015. Visualization and
641 analysis of dispersion process of combustible dust in a transparent Siwek 20-L
642 chamber. *J. Loss Prev. Process Ind.* 33, 213–221.

643 Dufaud, O., Vignes, A., Henry, F., Perrin, L., Bouillard, J., 2011. Ignition and explosion of
644 nanopowders: something new under the dust. *J. Phys. Conf. Ser.* 304, 012076.
645 <https://doi.org/10.1088/1742-6596/304/1/012076>

646 Eckhoff, R.K., 2012. Does the dust explosion risk increase when moving from μm -particle
647 powders to powders of nm-particles? *J. Loss Prev. Process Ind.* 25, 448–459.
648 <https://doi.org/10.1016/j.jlp.2011.11.011>

649 Eckhoff, R.K., 2011. Are enhanced dust explosion hazards to be foreseen in production,
650 processing and handling of powders consisting of nano-size particles? *J. Phys. Conf.*
651 Ser. 304(1), 012075. <https://doi.org/10.1088/1742-6596/304/1/012075>

652 EN 14034-1, 2004. Determination of explosion characteristics of dust clouds — Part 1:
653 Determination of the maximum explosion pressure P_{\max} of dust clouds.

654 EN 14034-2, 2006. Determination of explosion characteristics of dust clouds — Part 2:
655 Determination of the maximum rate of explosion pressure rise $(dp/dt)_{\max}$ of dust
656 clouds.

657 EN 14034-3, 2006. Determination of explosion characteristics of dust clouds — Part 3:
658 Determination of the lower explosion limit LEL of dust clouds.

659 European Commission, 2011. Recommendation on the definition of a nanomaterial
660 (2011/696/EU). Text with EEA relevance. Official Journal of the European Union

661 Hartley, P.A., Parfitt, G.D., Pollack, L.B., 1985. The role of the van der Waals force in the
662 agglomeration of powders containing submicron particles. *Powder Technol.* 42, 35–
663 46. [https://doi.org/10.1016/0032-5910\(85\)80036-X](https://doi.org/10.1016/0032-5910(85)80036-X)

664 Holbrow, P., Wall, M., Sanderson, E., Bennett, D., Rattigan, W., Bettis, R., Gregory, D.,
665 2010. Fire and explosion properties of nanopowders. UK Health and Safety, Executive
666 RR782.

667 ISO/IEC 80079-20-2, 2016. Explosive atmospheres — Part 20-2: Material characteristics —
668 Combustible dusts test methods.

669 Janès, A., Chaineaux, J., Carson, D., Le Lore, P.A., MIKE 3 versus HARTMANN apparatus:
670 Comparison of measured minimum ignition energy (MIE), *J. Hazard. Mater.* (2008).
671 <https://doi.org/10.1016/j.jhazmat.2007.06.066>.

672 Kalejaiye, O., Amyotte, P., Pegg, M., Cashdollar, K., 2010. Effectiveness of dust dispersion
673 in the 20-L Siwek chamber. *J. Loss Prev. Process Ind.* 23, 46-59.
674 <https://doi.org/10.1016/j.jlp.2009.05.008>

675 Kendall, K., 1988. Agglomerate Strength. *Powder Metallurgy* 31, 28–31.

676 Krietsch, A., Scheid, M., Schmidt, M., Krause, U., 2015. Explosion behaviour of metallic
677 nano powders. *J. Loss Prev. Process Ind.* 36, 237–243.
678 <https://doi.org/10.1016/j.jlp.2015.03.016>

679 Mehta, R.N., Chakraborty, M., Parikh, P.A. Impact of hydrogen generated by splitting water
680 with nano-silicon and nano-aluminum on diesel engine performance (2014) *Int. J.*
681 *Hydrogen Energ.*, 39 (15), 8098-8105. doi: 10.1016/j.ijhydene.2014.03.149

682 Murillo, C., 2016. Experimental and numerical approaches to particles dispersion in a
683 turbulent flow : application to dust explosions (PhD Thesis). Université de Lorraine,
684 France.

685 Oberdörster, G., Oberdörster, E., Oberdörster, J., 2005. Nanotoxicology: an emerging
686 discipline evolving from studies of ultrafine particles. *Environ. Health Perspect.* 113,
687 823–839. <https://doi.org/10.1289/ehp.7339>

688 Ogle, R.A. *Dust Explosion Dynamics* (2016) Butterworth-Heinemann, 1-639.

689 Rumpf, H., 1962. The strength of granules and agglomerates, *Agglomeration*. pp. 379–413.

690 Saeed, M.A., Farooq, M., Andrews, G.E., Phylaktou, H.N., Gibbs, B.M., 2019. Ignition
691 sensitivity of different compositional wood pellets and particle size dependence. *J.*
692 *Environ. Manage.* 232, 789–795. <https://doi.org/10.1016/j.jenvman.2018.11.122>

693 Sanchirico, R., Di Sarli, V., Russo, P., Di Benedetto, A. Effect of the nozzle type on the
694 integrity of dust particles in standard explosion tests (2015) *Powder Technol.*, 279, pp.
695 203-208. doi: 10.1016/j.powtec.2015.04.003

696 Santandrea, A., Bonamis, F., Pacault, S., Vignes, A., Perrin, L., Dufaud, O., 2019a. Influence
697 of the Particle Size Distribution on Dust Explosion: How to Choose the Right
698 Metrics? *Chem. Eng. Trans.* 77, 667–672. <https://doi.org/10.3303/CET1977112>

699 Santandrea, A., Pacault, S., Perrin, L., Vignes, A., Dufaud, O., 2019b. Nanopowders
700 explosion: Influence of the dispersion characteristics. *J. Loss Prev. Process Ind.*
701 <https://doi.org/10.1016/j.jlp.2019.103942>

702 Santandrea, A., Vignes, A., Krietsch, A., Brunello, D., Perrin, L., Laurent, A., Dufaud, O.,
703 2020. Evaluating the explosion severity of nanopowders: international standards
704 versus reality. *Process Saf. Environ. Prot.* 138, 279-
705 291. <https://doi.org/10.1016/j.psep.2019.12.018>

706 Sokolov, S.V., Tschulik, K., Batchelor-McAuley, C., Jurkschat, K., Compton, R.G., 2015.
707 Reversible or not? Distinguishing agglomeration and aggregation at the nanoscale.
708 *Anal. Chem.* 87, 10033–10039. <https://doi.org/10.1021/acs.analchem.5b02639>

709 Stark, W.J., Stoessel, P.R., Wohlleben, W., Hafner, A., 2015. Industrial applications of
710 nanoparticles. *Chem. Soc. Rev.* 44, 5793–5805. <https://doi.org/10.1039/C4CS00362D>

711 Walter, D., 2013. Primary Particles - Agglomerates - Aggregates, in: Deutsche
712 Forschungsgemeinschaft DFG (Ed.), *Nanomaterials*. Wiley-VCH Verlag GmbH &
713 Co. KGaA, Weinheim, Germany, pp. 9–24.
714 <https://doi.org/10.1002/9783527673919.ch1>

715 Weiler, C., Wolkenhauer, M., Trunk, M., Langguth, P., 2010. New model describing the total
716 dispersion of dry powder agglomerates. *Powder Technol.* 203, 248–253.
717 <https://doi.org/10.1016/j.powtec.2010.05.015>

718 Wu, H.-C., Chang, R.-C., Hsiao, H.-C., 2009. Research of minimum ignition energy for nano
719 Titanium powder and nano Iron powder. *J. Loss Prev. Process Ind.* 22, 21–24.
720 <https://doi.org/10.1016/j.jlp.2008.10.002>

721 Wu, H.C., Wu, C.W., Ko, Y.H. (2014). Flame phenomena in nanogrinding process for
722 titanium and iron, J. Loss Prev. Process Ind. 27, 114-118.
723 <http://dx.doi.org/10.1016/j.jlp.2013.11.002>

724